Spatio-temporal resource landscapes govern the confinement and escape of therapy-resistant mutants in structured populations

Nico Appold[1,2,4], Timon Citak[1,2,4], Auguste Palm[1,3], and Jona Kayser[1,2,*]

[1]Max-Planck-Zentrum für Physik und Medizin & Max Planck Institute for the Science of Light, 91058 Erlangen, Germany
[2]Department of Physics, Friedrich-Alexander-Universität Erlangen-Nürnberg, 91054 Erlangen, Germany
[3]Department of Biology, Chemistry, Pharmacy, Freie Universität Berlin, 14195 Berlin, Germany
[4]These authors contributed equally: Nico Appold, Timon Citak

December 22, 2025

1 Abstract

The ubiquitous evolution of therapy resistance remains a primary challenge for the durable control of pathological cellular populations, from microbial infections to cancer. In spatially structured populations such as biofilms and solid tumors, resistance-mediated therapy failure is driven not only by a continuous supply of *de novo* mutations and treatment selection, but by where resistant mutants arise relative to spatial resource gradients and how therapy reshapes these patterns. A fundamental mechanistic understanding of such couplings is essential to better predict therapy outcome and inform the principled design of spatio-evolutionary therapies. However, we currently lack experimentally tractable model systems that allow for a systematic, quantitative tracking of mutant emergence and expansion under time-modulated therapy in compact, range-expanding populations.

Here, we introduce a high-throughput microbial therapy-mimicry assay based on colonies expanded from single genetically-tailored yeast cells. This platform enables direct observation of the full spatio-temporal trajectories of continually emerging resistant clones under programmable treatment schedules.

Connecting experimental observations to an interpretable digital twin in a real-to-sim-to-real loop, we uncover an effective phase transition in metronomic schedule space that defines an optimal balance between population control with sustained resistance confinement, which we validate experimentally. Together, our results establish resource-mediated spatial confinement as a central organizing principle of resistance evolution and provide a mechanistic foundation for spatially informed, evolution-based therapies.

2 Introduction

The evolution of therapy resistance is a pervasive obstacle in treating pathological cellular populations, spanning bacterial infections, fungal pathogens, and cancer[1–4]. Resistance-mediated therapy failure is fundamentally driven by two coupled processes: the *de novo* emergence of resistant mutants during expansion and their subsequent amplification under

therapy. In well-mixed, mean-field descriptions, these processes can often be treated as separable: mutations supply resistant cells, and therapy reshapes relative fitness. However, many pathogenic populations are neither well mixed nor governed by spatially uniform conditions. Biofilms, tissues, and solid tumors are often compact, mechanically crowded, and structured by steep resource gradients. In such settings, resistance evolution becomes an intrinsically spatio-temporal process: where a mutant arises within the population and when selective pressure is applied can matter as much as the mutant's intrinsic fitness.

Over the past two decades, a broad body of work, often combining microbial evolution assays with spatial modeling, has shown that population structure and emergent collective phenomena fundamentally reshape evolution in dense, range-expanding populations. At expanding fronts, effective population sizes are small, competition is highly localized, and stochasticity is amplified [5–7]. Correlated founder effects can allow mutants to rise to unusually large frequencies simply by being in the right place at the right time, while growth-induced collective motion can modulate the power of selection itself[8–10]. Spatial effects can inflate the frequency of evolutionary "jackpot" events, generate intricate inflation-selection balances that maintain rare subclones, and facilitate evolutionary rescue by multi-step adaptation[11, 12]. In conjunction, these works demonstrate that evolution, including the emergence of drug resistance, needs to be described as an emergent process in such proliferating active matter systems[13]. Because continuous expansion concentrates evolutionary activity near the leading edge, much of this literature has focused on mutants that originate at or near the front. Recent work has begun shifting the focus to the mutant-rich bulk, a reservoir of many small, often undetectable mutant lineages[14]. However, these mutants can become evolutionarily decisive when environments change.

Considering therapy onset as a drastic environmental change builds a direct conceptual bridge between these insights and the emerging paradigm of evolution-based therapies. These approaches aim to exploit intrapopulation competition, maintaining a substantial sensitive population to suppress resistant cells, rather than attempting eradication at all costs[15, 16]. Such strategies were initially developed within mathematical models and have recently shown promise in preclinical studies and clinical pilot trials, with several larger trials in progress[17–21]. At the same time, spatially explicit simulations have demonstrated that local competition, spatial refugia, and heterogeneity in resource and drug fields can qualitatively change predicted outcomes compared to mean-field models[22–27].

Yet, despite the conceptual convergence between spatial evolutionary theory and evolution-based therapies, we currently lack experimentally tractable systems that allow for a systematic, quantitative probing of *de novo* resistance emergence and expansion under temporally modulated therapies in spatially structured, range-expanding populations. This limitation curtails our ability to uncover the fundamental mechanisms that shape therapy failure, test mechanistic hypotheses, and experimentally validate model predictions.

In this article, we address this gap by introducing a high-throughput microbial therapy-mimicry assay that enables direct observation of the full spatio-temporal trajectories of resistant clones in a range-expanding population under programmable treatment schedules. We then connect our empirical observations with a mechanistically interpretable "digital twin" and experimentally validate *in-silico*-optimized strategies in a real-to-sim-to-real loop.

3 Results

To quantitatively investigate the intricate interplay of the *de novo* emergence of resistance and the shifting population dynamics in response to therapy, we designed a well-controlled, high-throughput model system of colonies expanded from individual, genetically tailored *S. cerevisiae* cells (Fig. 1a). In addition, we introduced a multiplexed "synthetic mutation" system that couples a stochastic switch from a sensitive to a resistant phenotype with a shift in fluorescence color via a hierarchical dual-recombinase construct (Fig. 1b). In short, a tunable stochastic Cre/LoxP system triggers the mutation event. It deactivates

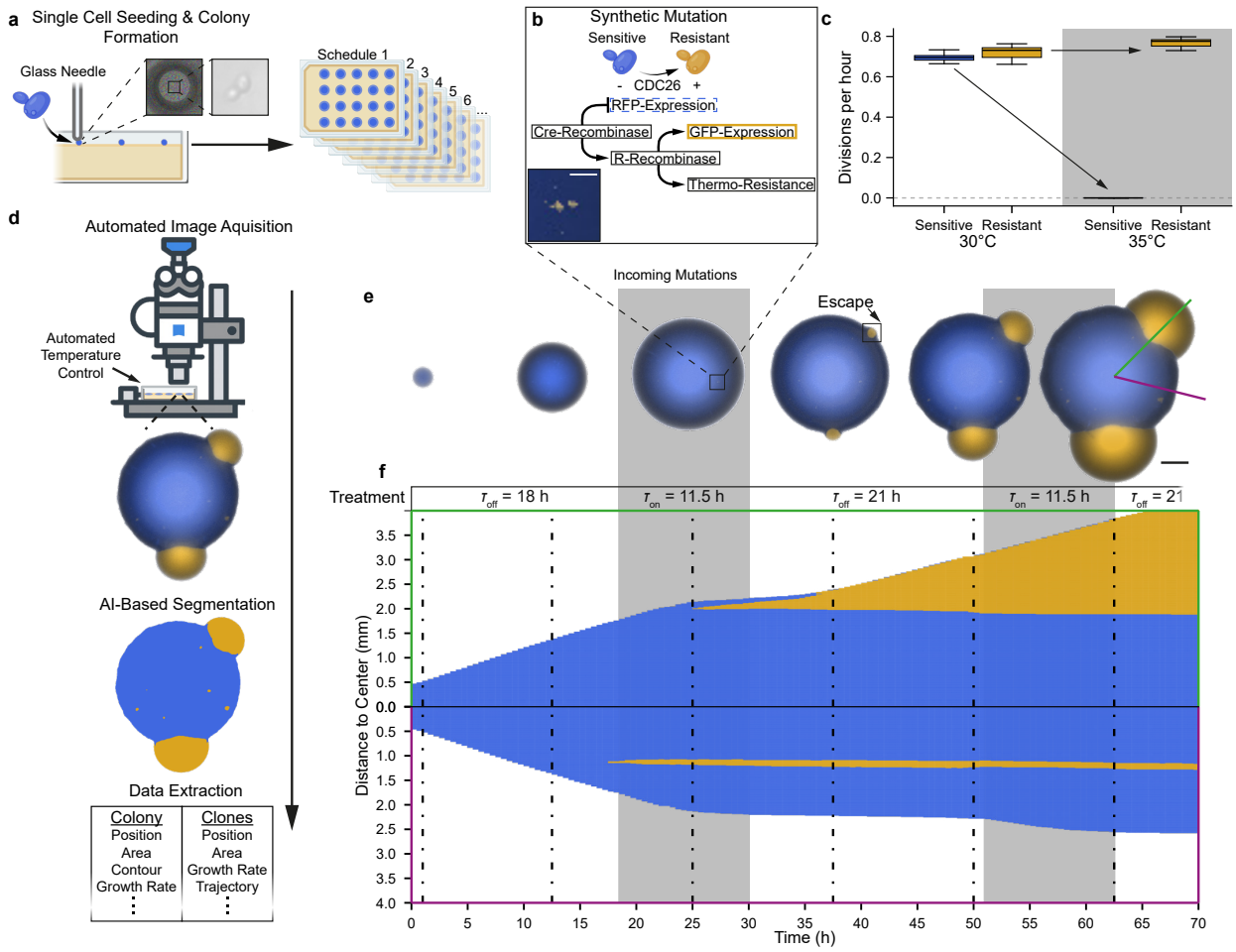

Figure 1: **Experimental setup to study resistance under time-structured treatment a)** Schematic of experimental workflow, starting from single-cell seeding of sensitive cells, followed by colony formation and time-lapse imaging under variable treatment schedules. **b)** Illustration of the synthetic mutation construct, in which the thermo-sensitive phenotype can stochastically undergo an irreversible recombinase-mediated switch to a thermo-resistant mutant. Scale bar indicates 100 µm. **c)** Maximal growth rates of sensitive and resistant subtypes at 30°C and 35°C. **d)** Overview of the image analysis pipeline, from automated time-lapse imaging to segmentation and measurement of colony- and clone-level data. **e)** Representative time-lapse images of a metronomic therapy experiment at the indicated time points. Imaging starts ($t = 0$h) 24 h after seeding. Resistant cells (yellow) expand as proliferation of sensitive population (blue) is arrested. Scale bar indicates 1 mm. **f)** Radial kymographs extracted from the colony depicted in **e** (colored radials), illustrating confinement and escape of bulk-born resistant mutants.

the initial expression of a red-fluorescing protein (depicted as blue) while simultaneously activating a secondary R-recombinase. The constitutive recombination of this secondary switch can then be used for a multiplexed activation of several open reading frame, such as *CDC26* and *GFP* (depicted in yellow) in our scenario, by excision of upstream stop codon cassettes.

With this system, we can emulate the differential fitness effects of therapy on sensitive and resistant cells using a thermo-resistance approach. Unmutated sensistive cells have an inactivated *CDC26* reading frame which allows for normal growth under low temperature conditions (30°C) but halts proliferation at elevated temperatures (35°C). Switching reactivates CDC26 expression, allowing mutated cells continued proliferation even at elevated temperatures (Fig. 1c).

This setup allows us to track the complete spatio-temporal trajectories of continually emerging resistant clones in populations expanded from single cells for up to 160 hours (> 100 generations) via multi-scale time lapse fluorescence microscopy (Fig. 1d). A computer controlled incubation system enables the execution of predefined treatment schedules.

To quantify intrapopulation dynamics, we built a custom segmentation and analysis pipeline that automatically extracts both colony scale and clone level data, such as size, position, and contour, over the entire population history. Fig. 1e shows an example time series with two treatment pulses. A kymograph-like presentation of the segmented data facilitates visualization of the population dynamics within a selected radial (Fig. 1f, colored radials in e). We find individual clones emerging at different radial positions throughout population expansion. Upon treatment initiation the growth of the sensitive population gradually comes to a halt while resistant clones begin to expand. After treatment is discontinued, sensitive cells only slowly begin to resume growth. While some resistant clones remain confined within the population bulk, others expand to the colony edge, permanently escaping confinement as continually growing domes. In this spatial setting, whether a clone remains confined or escapes appears to depend on its relative position within the colony.

3.1 Continuous therapy releases resistant mutants from spatial resource confinement

We hypothesize that this spatial confinement is primarily mediated by the local scarcity of resources within the population bulk, rather than directly by crowding [9, 11].

To quantitatively test this resource-confinement-hypothesis, we measured how new resistant clones emerged under continuous therapy (CT) (Fig. 2a). In this strategy, we first expanded colonies at 30°C (therapy off) and then increased temperature to 35°C, where we held it for the remainder of the experiment. If the availability of nutrients is indeed the mechanism of confinement, their diffusive redistribution after sensitive cell growth is stopped should result in mutants first emerging close to the population front, followed by growth deeper in.

Recording the time and position at which mutant clones are initially detected, we indeed observe a strong correlation between the time a mutant is first detected and its distance from the colony front (Fig. 2b). In addition, we can track the trajectory of individual clones (Fig. 2c-d). While some deeper clones become trapped behind another resistant mutant growing in front of them (Fig. 2c, gray traces in d), escaping clones follow a typical trajectory towards the edge. Tracking how their distance to the front changes, we find that each clone initially accelerates but then continues to decrease its distance at a near-constant velocity until escaping (Fig. 2d, red traces).

These findings not only corroborate our resource-confinement-hypothesis, they also show that the positional and temporal patterns of resistant mutant escape are intrinsically linked. The time after therapy onset it takes a resistant clone to permanently escape is governed by its initial position in two ways: The time it takes sufficient amounts of nutrients to diffuse to this position from the outside and the time it takes the expanding clone to reach the colony edge and escape. This dynamic is also captured by the continually increasing cumulative count of escaped resistant clones per colony (Fig. 2e).

3.2 Resistant mutants can be reconfined by stopping therapy

The observed window between treatment start and resistance escape could, in principle, offer the possibility to apply a short treatment pulse that reduces overall population expansion while maintaining the

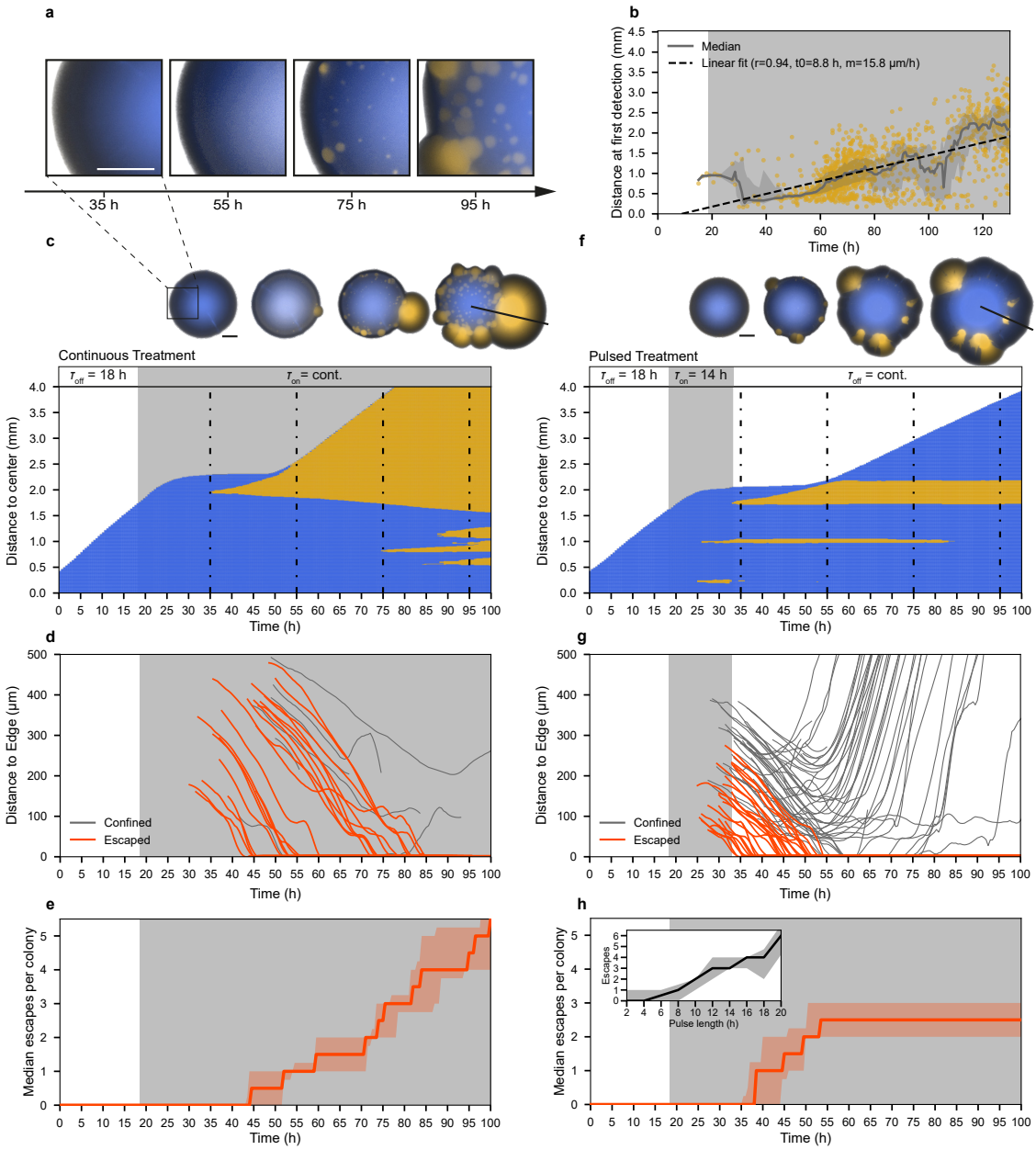

Figure 2: **Therapy pause can reconfine resistant clonesa)** Illustrative time-lapse images highlighting the expansion of resistant clones during treatment **b)** Distance of resistant clones from the colony front at first detection during continuous therapy **c,f)** Radial kymographs and corresponding time-lapse images for continuous (c) and pulsed (f) treatment schedules. **d, g)** Trajectories of the front-most position of individual resistant clones over time under continuous (d) and pulsed (g) treatment. **e, h)** Median cumulative number of escaped resistant clones per colony under continuous (e) and pulsed (h) treatment. Inset: Median cumulative number of per-colony escape events for different pulse durations. Scale bars indicate 1 mm

confinement of resistant mutants. Testing this notion, we initiated treatment as before, bringing colony expansion to a halt. However, we then stopped treatment after a pulse duration of $\tau_{\text{on}} = 14$ h, resuming sensitive cell growth (Fig. 2f).

During the short treatment pulse, no clone had escaped by the time of treatment interruption. However, due to a extended delay in the rebound of sensitive population expansion, some clones still escaped before growth was fully resumed. Still, the largest portion of resistant clones eventually receded back into the population bulk without further escapes (gray traces in Fig. 2g, h). Modulating the pulse duration, we find that resistance confinement can be further enhanced by shortening the pulse length (Fig. 2h, inset). For pulses of $\tau_{\text{on}} < 6$ h, escapes all but vanish.

These observations are in line with our initial hypothesis that diffusive redistribution of resources under treatment is at the root of resistant mutant escape. However, directly measuring the nutrient landscape and its dynamic reshaping under time-modulated therapy is infeasible in experiments.

3.3 An *in silico* twin couples nutrient landscape dynamics to resistant mutant escape

To systematically explore the dynamics of resource-confinement and release, we designed a stochastic simulation framework to act as a "digital twin" of our experiments in which the nutrient landscape is readily accessible. These simulations spatially integrate nutrient-dependent proliferation with growth-driven cell dispersal and nutrient diffusion in two dimensions (Fig. 3a).

In short, space is divided into a 2D grid of demes, each containing a mixture of susceptible cells S and resistant cells R that proliferate at rate α, mutate at rate μ and disperse with an effective diffusion coefficient D (Fig. 3b). To emulate the growth-dependent mutation and dispersal of our experiments, these processes are only applied to the actively growing per-deme populations of sensitive and resistant cells $S_{\text{d}} = \alpha\xi NS$ and $R_{\text{d}} = \alpha NR$, respectively:

$$\frac{\partial S}{\partial t} = S_{\text{d}} + D\Delta S_{\text{d}} - \mathcal{M}_{\mu}(S_{\text{d}})\,, \tag{1}$$

$$\frac{\partial R}{\partial t} = R_{\text{d}} + D\Delta R_{\text{d}} + \mathcal{M}_{\mu}(S_{\text{d}})\,. \tag{2}$$

Experimentally observed delays in treatment effects on growth rate are implemented via the the therapy induced growth rate modulation $\xi \in [0, 1]$, exhibiting an on-delay, lag-delay and off-delay (Fig. 3c). Stochastic mutations are randomly sampled from a Poisson distribution $\mathcal{M}_{\mu}$ defined by the expectation value $\mu \cdot S_{\text{d}}$.

Importantly, competition is solely mediated via nutrient limitation without introducing a local carrying capacity (Fig. 3b). Nutrients are modeled as a freely diffusing consumable resource with the diffusion coefficient D_{N}:

$$\frac{\partial N}{\partial t} = D_{\text{N}}\Delta N - \gamma(S_{\text{d}} + R_{\text{d}})\,, \tag{3}$$

with γ being the consumption rate of nutrients. To better visualize the therapy-induced shifts in nutrient availability, we also compute the width λ of an effective growth layer that integrates all available nutrients into the peripheral region at a constant concentration (Fig. 3d).

Using the parameterized model, we simulated population trajectories for both continuous treatment and a 14 h treatment pulse (Fig. 4d,e). Despite their simplicity, the simulations are able to qualitatively capture the key spatio-temporal dynamics observed in colony experiments, including competitive release of internal resistant clones and the ability to maintain confinement by pausing treatment in a duration dependent manner (Fig. 4e, f). Moreover, we can now directly tie these dynamics to the shifting nutrient landscape (Fig. 4g, h). After treatment initiation, the effective growth layer gradually extends deeper into the colony, facilitating the growth of previously nutrient deprived resistant clones. For continuous treatment, this retrograde shift inevitably leads to the escape of resistant mutants which then expand with a reestablishing growth layer width (Fig. 4g). For a treatment pulse, in contrast, the λ is only increased temporarily. If clones are sufficiently far away

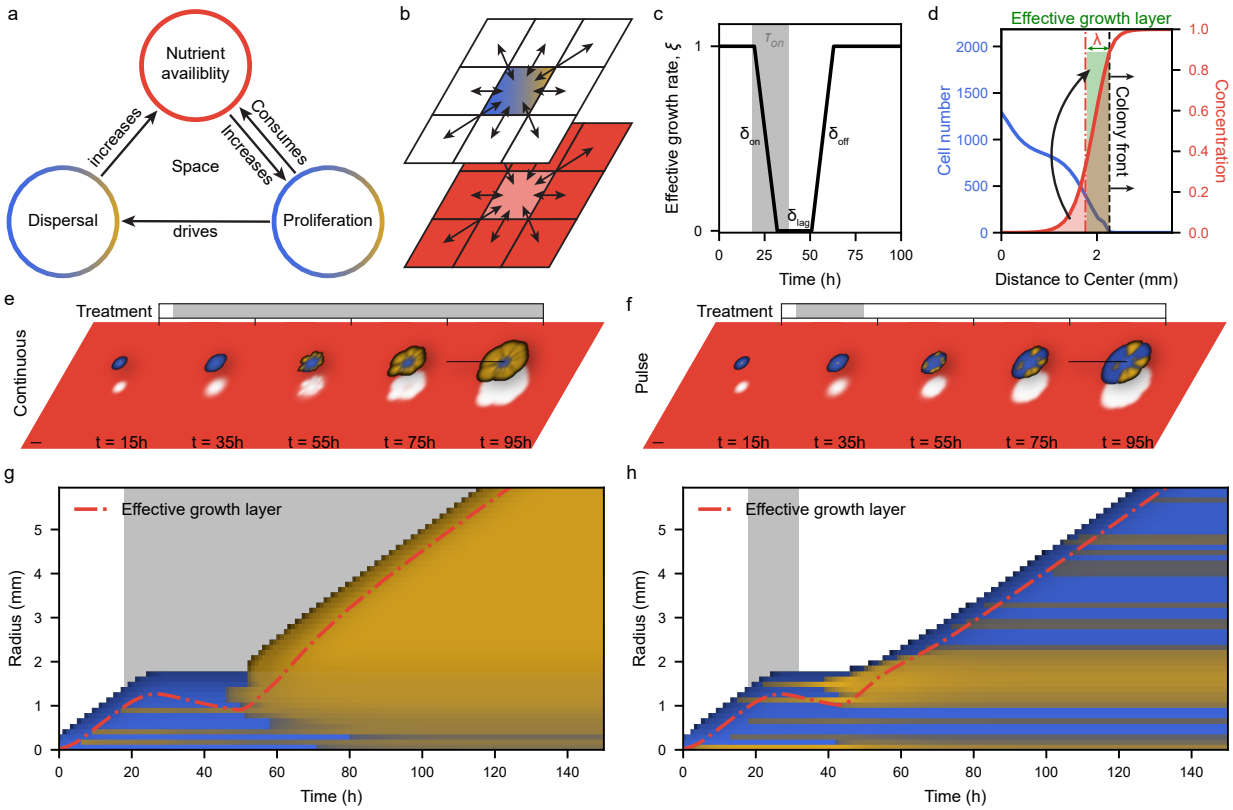

Figure 3: **An effective nutrient-mediated growth layer governs resistance confinement and escape in a digital twin. a)** Schematic of spatial couplings between nutrients, proliferation and dispersal. **b)** The simulation consists of sensitive (blue) and resistant (yellow) populations interacting with each other via an underlying nutrient landscape (red), organized on a 2D square lattice. **c)** Treatment modifies growth rates with delay, leading to an effective growth rate ξ. The specific form of the modification is defined by 3 parameters: δ_{on}, the time it takes for treatment to take full effect, δ_{lag}, the time ξ stays constant after treatment ends, and δ_{off}, the time it takes until ξ fully recovers. **d)** The extend of the continually declining nutrient gradient can be visualized by integrating all nutrients into an effective growth layer of width λ with constant concentration. **e), f)** Time lapse of a continuous dose and a 14 h pulse simulation run. The black line marks the position of the kymograph in f. Scale bar indicate 2 mm. **g), h)** Kymograph-like diagrams for the continuous dose and pulse treatments in e and f, showing the effective growth layer trajectory.

from the edge or the pulse duration is sufficiently small, the growth layer width decreases again before the resistant clones can escape (Fig. 4h), keeping it confined.

Combining these insights with our empirical data we can summarize the mechanisms defining resistant clone confinement or escape as follows: Depending on the local availability of nutrients, cells grow and divide, consuming nutrients in the process. In a non-spatial scenario, this feedback would result in logistic growth dynamics. In the spatially structured colonies studied here, however, proliferation is intrinsically linked with cell dispersal. Together, this results in a spatial nutrient gradient along the direction of colony expansion. Without therapy, growth-driven dispersal of cells up this gradient increases the nutrient availability at the leading edge of the colony, resulting in continuous expansion [5, 9, 11]. Treatment onset destabilizes this configuration. As sensitive cells cease to consume resources, nutrients gradually get redistributed down the concentration gradient via diffusion. This shift, if continued, results in the growth and eventual escape of resistant clones, growing up the gradient. However, limiting this inward motion of the nutrient gradient by halting treatment can mitigate resistant mutant escape.

While discontinuation of treatment facilitates the confinement of resistant clones, these gains come at the cost of continued colony expansion and yield little gain in minimizing overall population growth. A series of short but regular treatment pulses and pauses, often referred to as metronomic therapy (MT), should, in principle, be able to better balance mutant confinement with overall colony expansion. However, how such a balance is shaped by the emergent effects of spatial population structure and its coupling to a varying nutrient landscape under therapy is unclear. Systematically probing the parameter space of treatment interval combinations directly in experiments is logistically infeasible.

We therefore first use the digital twin as a guide by probing a large parameter space of combinations of fixed treatment application and pause duration $\boldsymbol{\tau} = (\tau_{\text{on}}, \tau_{\text{off}})$. We define the time it takes for the population to progress beyond a predefined area threshold of 71 µm^2 as a metric for therapy outcome. Quantifying this time to progression (TTP), we find two distinct regimes of early progression, separated by a line of maximum TTP, $\boldsymbol{\tau}^*$ (Fig. 3a). These two "phases" show distinct differences in variability (Fig. 3b). Measuring the relative fraction of resistant clones at progression, identifies each phase as being either dominated by sensitive (undertreatment) or resistant cells (overtreatment), with a sharp transition at the line of maximum TTP (Fig. 3c).

Isolating the effects of treatment duration by holding the pause duration constant (Fig. 3d, colored dashed lines in a-c), we find that short τ_{on} yield good confinement of resistant mutants with a low frequency of resistant cells but early progression due to sensitive cell growth. Increasing τ_{on} initially extends the time to progression. However, there is a maximum TTP at τ_{on}^* after which further increases result in decreases in TTP accompanied by a rapid increase in mutant frequency. In other words, $\boldsymbol{\tau}^*$ optimally balances reduction of sensitive cell growth and mutant confinement. Interestingly, the TTP maximum becomes much less pronounced for longer τ_{off}.

To unravel the processes driving the observed outcomes, we analyzed the population trajectories for a fixed $\tau_{\text{off}} = 18$ h at both sides of the TTP maximum as well as just before mutant frequency increases (Fig. 3, e-g, colored markes in a-c, $\tau_{\text{on}} = 4$ h, 6.5 h, 9 h). Specifically, we measured how the subpopulation areas evolve over time, as well as their respective area growth rates and the resistant mutant fraction.

We find that for short treatment intervals ($\tau_{\text{on}} = 4$ h) population expansion not only recovers after each treatment cycle but increases over time with mutants remaining efficiently confined (Fig. 3e-g, first column). This rebound remains similar for intermediate pulse durations ($\tau_{\text{on}} = 6.5$ h), but with a more pronounced decrease in sensitive cell growth within each cycle (Fig. 3e-g, second column). However, further increasing the pulse duration ($\tau_{\text{on}} = 9$ h) qualitatively changes the dynamics. Growth does no longer rebound completely, introducing a hysteresis (Fig. 3e-g, third column). Each successive cycle decreases the growth rate further, leading to strong suppression of sensitive cell growth and, consequently, the abundant escape of resistant clones. The kymograph-like sections in Fig. 3h illustrate how minute changes in

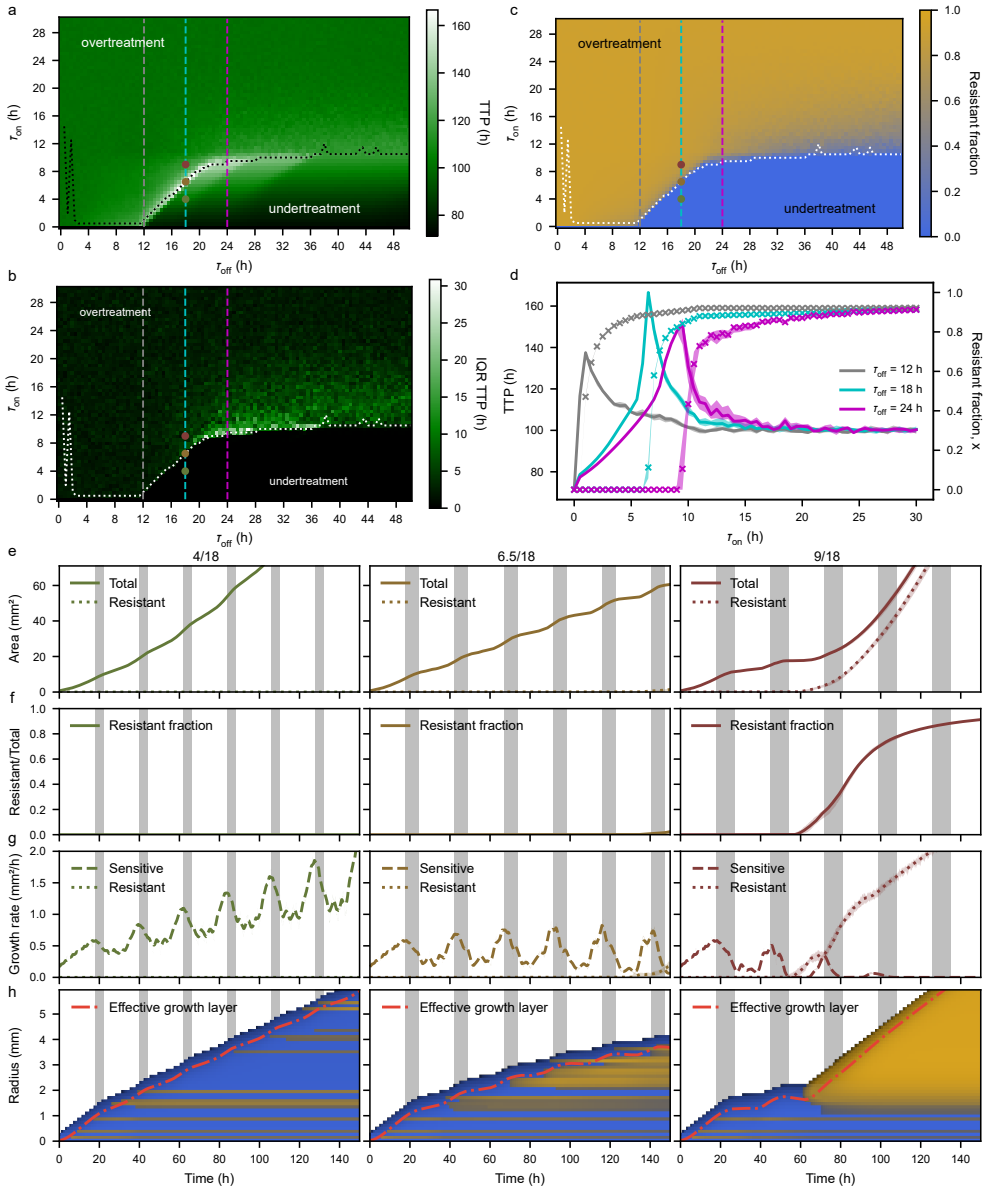

Figure 4: **An effective phase transition in treatment space defines therapy outcome. a)** Parameter sweep over treatment on τ_{on} and off τ_{off} pairs showing the median optimal time to progression (TTP) regimes (n = 20 runs for each pair). Colored dots mark the schedules shown in e. Dashed vertical lines correspond to the profiles shown in d. The dotted line shows the maximum TTP position for each τ_{off} value.**b)** Interquartile range for the TTP depicted in a). **c)** Median resistant fraction for the same sweep. **d)** Example profiles TTP and the resistant fraction profiles together with their respective IQR. **e) - g)** Median area trajectory, median area growth rates, and median resistant fraction trajectories for the treatment schedules $\tau_{\text{on}} = 4\,\text{h}, 6.5\,\text{h}, 9\,\text{h}$ and $\tau_{\text{off}} = 18\,\text{h}$. The marked area is the IQR (n = 20). **h)** Kymograph-like diagrams together with the effective growth layer position for one example angle and simulation run of the above schedules.

the depth of growth layer undulations can lead to very different population trajectories.

Such a strong change in system state due to a small change of an input parameter is reminiscent of a phase transition. While our system is always far from equilibrium, required for a true phase transition, we can use this context as a conceptual framework to understand the observed biphasic therapy outcome.

Leveraging our mechanistic understanding of mutant escape dynamics we can now rationalize why the spatial structure of the population and its collective growth dynamics are so essential. It allows for a substantial temporary reduction of sensitive cell growth without jeopardizing the confinement of *de novo* resistant mutants. The strong positional advantage of sensitive cells residing between an internal resistant mutant and the colony edge can compensate for a substantial reduction in growth. As a result, sensitive growth can be reduced without loss of confinement within one cycle. For $\tau_{\text{on}} < \tau_{\text{on}}^*$, growth can always rebound so that each new cycle can be considered independent of the previous one, equivalent to a Markovian reset. In this scenario, the cycle-averaged growth rate $\overline{\xi}$ remains sufficiently high to maintain a shallow growth layer that keeps resistant mutants confined.

However, for $\tau_{\text{on}} > \tau_{\text{on}}^*$ the rebound remains incomplete, introducing hysteresis. The resulting non-Markovian dynamics cause a cumulative drop of $\overline{\xi}$ to values at which resistance confinement can no longer be maintained. Together, these two emergent phenomena, the phase transition in treatment effect and the enhanced spatial confinement of resistant clones, are the only key ingredients necessary to describe the observed complex therapy response, including the optimal balance.

It is important to emphasize that the simplified digital twin cannot quantitatively capture all experimentally observed dynamics in detail. For example, the exact position of the phase boundary is very sensitive to the changes in the shape of therapy response delays, which is non-trivial in experiments. Any quantitative predictions should therefore be only considered as rough guides. Nonetheless, the basic mechanisms underlying the optimal balance argument above are so fundamental that they should still apply in a more complex experimental scenario.

3.4 Experimental validation of optimal metronomic therapy

Guided by the digital twin, we tested the observed principles empirically by applying a set of metronomic schedules $\boldsymbol{\tau} = (\tau_{\text{on}}, \tau_{\text{off}})$ in experiments. Holding $\tau_{\text{off}} = 18$ h constant, we probed the dynamics at both sides of the predicted phase transition by varying τ_{on} (4 h, 6.5 h, 9 h), as well as no-treatment and continuous treatment references (Fig. 5a).

Comparing overall therapy performance by measuring the time to progression (TTP) and resistant fraction, we find a characteristic optimality very similar to that observed in the digital twin (Fig. 5b, c). TTP initially increases with longer treatment duration but then peaks at $\tau_{\text{on}} = 6.5$ h (Fig. 5c). This peak also correlates with a sudden rise in mutant abundance (Fig. 5d).

Measuring how the area of sensitive and resistant cell population changes over time, analogous to the analysis of simulation data in Fig. 3, we find a behavior that qualitatively matches that observed in the digital twin. For short treatment durations ($\tau_{\text{on}} = 4$ h), therapy induced growth rate reductions of sensitive cells are balanced by a rebound of growth during therapy pauses, resulting in a slowly increasing cycle-averaged growth rate and strong confinement of resistant mutants (Fig. 5e). For $\tau_{\text{on}} = 6.5$ h, the cycle-averaged growth rate remains almost constant throughout the experiment, paired with a noticeable but still small increase in resistance fraction. Intriguingly, with $\tau_{\text{on}} = 9$ h, experiments indeed exhibit the cumulative decrease in sensitive cell growth and the surge in mutant escapes that is characteristic for the resistance dominated phase (Fig. 5f, g, h).

While these empirical results only cover a very small, albeit critical, part of the therapy space, they are strong evidence that the concept of a therapy dependent phase transition also applies to the much more complex experimental realm. Moreover, they are a direct demonstration that the intrinsic coupling between spatial population structure and a therapy-modulated nutrient landscape can be exploited for therapy optimization while concomitantly making it

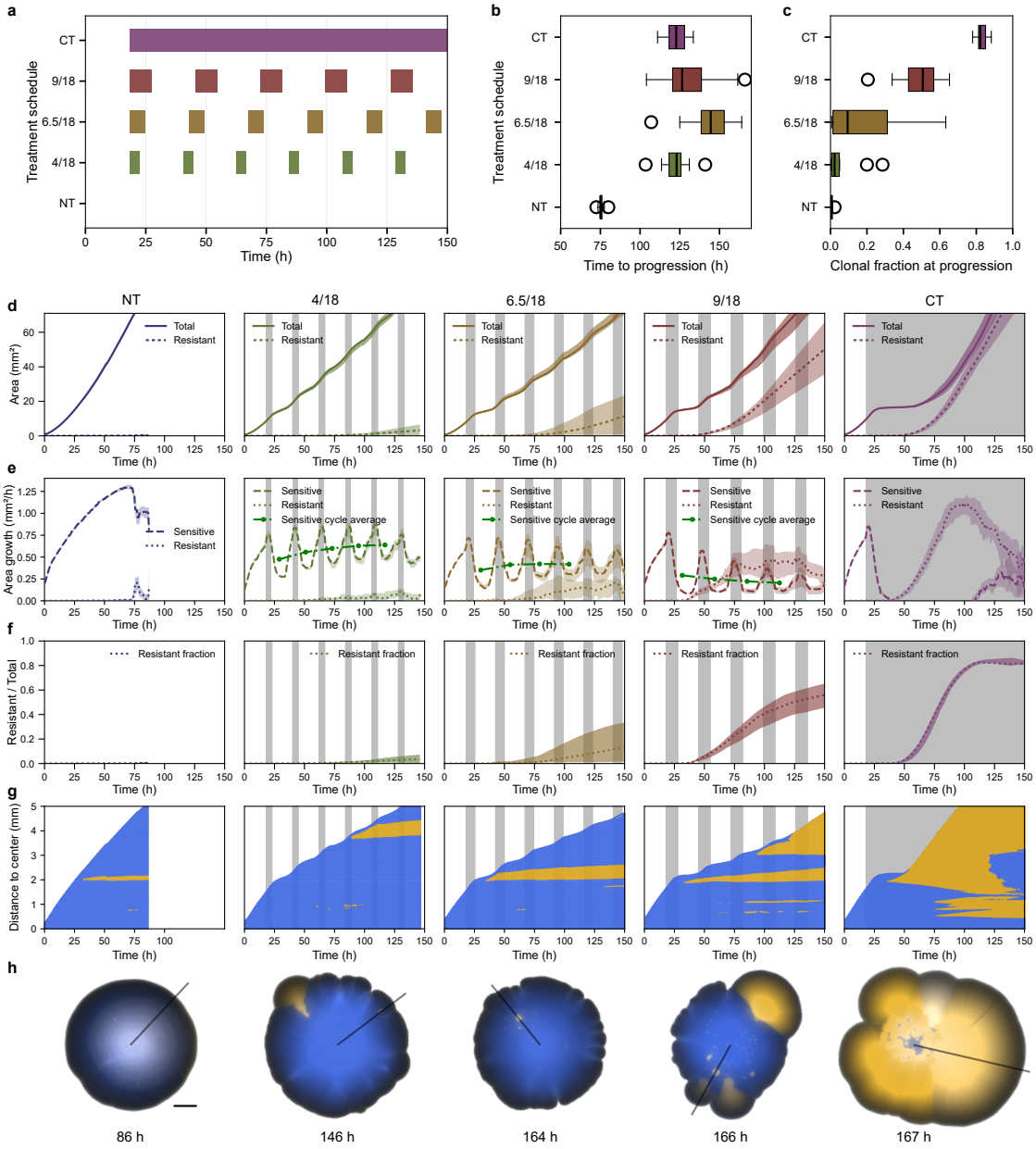

Figure 5: **Experiments support simulated treatment schedules that delay progression a)** Experimentally tested schedules and their corresponding τ_{on} intervals **b)** Time to progression (colony area $\geq$ 71 mm^2) for the tested treatment schedules. **c)** Clonal fraction for colonies at time to progression. **d)** Median total colony area and resistant area for no treatment (NT), metronomic schedules ($\tau_{\text{on}}/\tau_{\text{off}}$: 4/18, 6.5/18, 9/18), and continuous treatment (CT). **e)** Area growth dynamics of sensitive and resistant populations, including the cycle-averaged growth of the sensitive population under the indicated treatment schedules. **f)** Temporal evolution of the resistant fraction throughout the experiment. **g)** Radial kymographs of representative colonies for the indicated treatment schedules (cf. black radial lines in h). **h)** Representative colony images at the experiments final image corresponding to the kymographs shown in g. Scale bar indicates 1 mm

challenging to hit the therapeutic sweet spot of optimal balance.

4 Discussion

In structured populations, resource fluxes are a prime determinant of spatial growth patterns. Therapy can transiently disrupt these patterns, resulting in the escape of previously confined resistant mutants from the population bulk.

To systematically study the processes that govern these dynamics, this work introduces a therapy mimicry assay based on a genetically tailored yeast model. Pairing empirical results with an experiment-parameterized digital twin in a real-to-sim-to-real approach, we probe a large therapy design space, identify a metronomic therapy schedule that optimally balances population growth and resistance confinement, and then verify this *in silico*-derived strategy in experiments.

Three main conceptual insights emerge from this study: First, therapy-induced nutrient redistribution can drive resistant mutant escape and therapy failure in spatially structured populations. This underlying key mechanism can be conceptualized via an effective peripheral growth layer λ that shifts in response to therapy. Second, strategically pausing treatment can be leveraged as a general control principle by mitigating or even reversing these λ-shifts. Resistance confinement can be maintained if λ does not exceed a critical value. Third, small changes in treatment duration can cause dramatic changes in therapy outcome by switching from a Markovian to a non-Markovian treatment response class. The resulting effective phase transition defines a narrow therapeutic sweet spot that is completely characterized by treatment on and off kinetics.

The fundamental nature of the uncovered mechanisms suggests that similar effects may be present in a much wider class of spatially structured populations with resource gradients, including many bacterial biofilms and solid tumors. A broad collection of previous work has shown how emergent spatial and physical phenomena reshape the evolutionary dynamics at the expanding front of these systems[5, 7, 9–12, 28]. Our work builds on these insights by showing that shifting fitness landscapes, with modulated therapy being an extreme example, can transiently shift the effective growth front to the mutant-rich population bulk, drastically increasing the genetic diversity accessible to evolution. Strategically controlling intrapopulation competition is foundational to the new paradigm of evolution-based tumor therapies[15, 18, 24, 25]. In this context, our findings offer a new perspective on how the inherent resource gradients in solid tumors may be optimally exploited for improved therapy design. For example, poorly vascularized tumor types, often associated with steep gradients and resource-depleted core regions, appear as ideal candidates for adaptive therapies. Complementary treatments targeting angiogenesis, such as VEGF inhibitors, may further enhance the effectiveness of such therapy strategies. In addition, our results may offer a new rationale explaining why recent clinical trials of metronomic therapy in metastatic melanoma did not improve progression-free survival in patients, despite strong preclinical evidence[29]. Finding the narrow therapeutic sweet spot is inherently challenging due to the biphasic nature of the therapy space while the commonly applied lead-in phase may eradicate it altogether.

While the effects observed in our well-controlled microbial model system might be general in nature, there will be additional influences on the evolution of resistant subclones in more complex systems. For example, both bacteria and tumor cancer cells actively migrate and interact with each other in a complex 3D microenvironment. In addition, our work primarily discusses therapy trajectories for individual populations, while systemic therapies, including evolution-based tumor therapy, is most relevant in a metastatic scenario with multiple heterogeneous lesion sites. It should also be noted that for both, antibiotic and anti cancer therapies, treatment typically causes cell death rather than the reversible inhibition of growth studied here. It will be therefore quintessential to additionally test the nuances of resource-mediated spatial confinement and derived therapy strategies in more realistic model systems that better capture these complexities, such as cancer cell organoids or biofilms of matrix-producing bacteria.

In conclusion, our work underscores the critical role of an inherent spatio-temporal coupling between therapy-modulated nutrient landscapes, mutant growth and their escape in densely packed cellular populations. In essence, therapy failure risk is governed by whether therapy shifts the resource gradient long enough for bulk-born mutants to permanently escape confinement. Integrating the gained insights into our understanding of resistant evolution and therapy response will open new avenues for combating resistance-mediated therapy failure.

5 Methods

5.1 Strains

All experiments were performed using the genetically engineered strain yNA16 of the budding yeast *Saccharomyces cerevisiae*. yNA16 is derived from the ancestor strain yJK19 and carries a β-estradiol-inducible Cre-EBD recombinase expressed from the *SCW11* promoter and integrated at the *HO* locus. yNA16 harbors a synthetic, irreversible recombination-based mutation cassette (*PGPD-loxP-yEmRFP-ubq-cyh2r-TCYC1-kanMX-loxP-yEGFP-ubq-Rrec*), enabling stochastic switching from a sensitive to a resistant state accompanied by a fluorescent color change.

Thermosensitivity was introduced via an auxotrophic insertion at the *CDC26* locus (*pCDC26-RS-URA3-tURA3-RS-CDC26*). To enhance fluorescent signal in the switched state, a second activatable GFP cassette (*pGPD-RS-LEU2-tLEU2-RS-yEGFP-tADH*) was integrated. A switched derivative strain (yNA16s) was generated by inducing Cre activity with 3 µM β-estradiol in liquid culture, followed by selection at 35 °C. A resistant clone exhibiting stable green fluorescence was isolated and used for downstream experiments.

5.2 Construction of yNA16

yNA16 was generated through sequential genetic modifications of yJK19. First, the Cre-responsive switching cassette was integrated to generate yNA14. Thermosensitivity was subsequently introduced at the *CDC26* locus, yielding yNA15. Finally, an additional recombination-activated GFP cassette was inserted to improve fluorescence intensity in the switched state, resulting in yNA16. All genetic constructs were amplified by PCR and assembled using NEBuilder HiFi DNA Assembly (New England Biolabs).

5.3 Yeast Transformation

Yeast transformation were performed using lithium acetate/polyethylene glycol (LiAc/PEG)-based protocol. Yeast strains were inoculated into 5 ml YPD and grown overnight at 30 °C. The follwoing day, cultures were diluted into 50 ml YPD to an initial OD_{600} of 0.2 and grown at 30 °C with shaking for 3-4 h until reaching OD_{600} of $\tilde{1}.0$. Cells were harvested by centrifugation (300 x g, 5 min), washed once with sterile distilled water, and resuspended in 1 ml distilled water. Aliquots of 100 µl were pelleted and resuspended in a transformation mix containing 50 % (w/v) PEG 3500, 1.0 M lithium acetate, boiled single-stranded carrier DNA, and either PCR product DNA or plasmid DNA. Cells were incubated at 42 °C for 40 min, pelleted, and gently resuspended in 250 µl YPD. Transformants were plated on YPD agar or selective media and incubated at 30 °C. For antibiotic selection, colonies were replica-palted onto YPD plates containing the corresponding antibiotic after overnight recovery.

5.4 Measuring growth rate

Growth rates of yNA16 and yNA16s at 30 °C and 35 °C were determined using plate reader assays. Thin liquid cultures were diluted 1:1000, and 10 µl of each culture was added to 450 µl of YPD per well in a 48-well plate. Each strain was measured in 16 replicates per plate, with OD_{600} recorded every 10 min. Plates were continuously shaken during incubation to promote exponential growth of all cells in suspension. Doubling times were estimated by fitting an exponential curve to the growth trajectories. The experiment at 30 °C was repeated twice to account for stochastic variation.

Name or Schedule ($\tau_{\text{on}}/\tau_{\text{off}}$)	No. Colonies
No treatment	13
Continuous treatment	9
Pulse (14 h)	12
4/18	10
6.5/18	13
9/18	10

Table 1: **Number of colonies acquired in all experimental approaches**

5.5 Population assay

For the standard population assay, *yNA16* populations were pre-cultured on YPD + 2 % agar supplemented with 200 µg/ml G418 for 2 days, then stored at 4 °C for up to 3 weeks. Monoclonal colonies from these plates were used to inoculate 3 ml liquid YPD medium containing 200 µg/ml G418 and grown for approximately 5 h at 30 °C. Cultures were vortexed for 5 min to disperse cell clusters, and 30 µl were spread in a narrow band on one side of a monowell plate containing 70 ml of 1 % agar YPD. The Plates were dried under sterile conditions with the lid open for 45 min prior.

Single cells, preferentially with a small bud, were isolated using a Singer MSM400 dissection microscope and placed in a 5 × 4 grid, yielding a potential maximum of 20 colonies per plate. Plates were incubated at 30 °C and 85 % relative humidity for 24 h to allow initial colony expansion, after which they were transferred to an on-stage incubation chamber for time-lapse imaging. Multichannel images were acquired every 30 min for up to 7 days. Temperature-based treatments and therapy holidays were implemented by adjusting the incubation chamber temperature manually or via a pre-programmed script. A type K thermocouple, placed on the agar surface at colony height, was used to monitor on-plate temperature. Colonies that showed petite mutations or had contamination were excluded from analysis. Tab. 1 shows a summary of all conducted experiments.

5.6 Imaging and analysis

Imaging was conducted using a AxioZoom V16 fluorescence microscope from Zeiss with a Objective Apo Z 1,5x/0,37 at a total magnifiaction of 10.5 over the whole time span of an experiment. Final images were taken using the PlanApo Z 0.5x objective at a total magnification of 6.3. As software for the acquisition we used Zen Blue 3.0. Pictures were than analyzed using a row of Python 3.11 scripts and Ilastik, a machine learning based image segmentation tool, trained on time spaced frames of randomly picked colonies[30]. All time lapse data shown was segmented with the same segmentation model, the final images were segmented using a separate model to ensure consistency. For displaying pictures and adjusting colormaps, Fiji was used on the raw imaging data.

5.7 Clonal Tracking

Clone trajectories were filtered to restrict the analysis to comparably emerging and reliably tracked clones. Only clones whose first detection occurred between frames 50 and 100 were included, excluding early-appearing clones and late detections with insufficient temporal coverage. From this subset, clones were required to enter a defined spatial band relative to the colony front at least once during their lifetime, with distances constrained between 2 and 30 pixels. This criterion restricted the analysis to clones originating within the actively growing region of the colony and excluded both central and edge-contact artefacts. Clones were further required to be tracked for a minimum of three consecutive frames.

Distances to the colony edge were converted to physical units using a scale factor of 8.648 µm per pixel. Clones were classified based on their interaction with the colony front: a breach was defined as reaching a distance of ≤ 20 µm from the colony edge at least once. Following a breach, clones were classified as *escaped* if they did not subsequently retreat beyond 80 µm from the colony edge, whereas clones that never breached or retreated beyond this threshold were classified as *confined*. For visualization purposes only, trajectory traces were smoothed using a

Savitzky-Golay filter; all classification decisions were based on unsmoothed data.

5.8 Time-to-progression and extrapolation

To enable consistent determination of time to progression based on a fixed maximal colony area (corresponding to the area a perfectly round colony can occupy in the absence without imaging related truncation), colony- and clone-area trajectories were extrapolated when growth extended beyond the field of view. Under treatment, resistant clones could expand asymmetrically and partially leave the imaging frame, leading to an underestimation of clonal area. For each colony, the first time point at which the colony contour contacted the image border was detected, and the last trusted measurement was defined as the preceding frame. From this frame onward, colony area and total clonal area were extrapolated linearly in physical to a final target area measured from a corresponding endpoint image acquired at a lower magnification. The endpoint was assigned to a time point one frame after the last time-lapse frame. No extrapolation was applied to the no-treatment condition, as colonies reached the time-to-progression threshold without leaving the imaging frame.

5.9 Simulation

We built a custom 2D lattice simulation consisting of sensitive and resistant cells interacting via a nutrient layer. The sensitive cells can mutate into resistant cells. The simulations are performed on a 200 $\times$ 200 grid, where the cells have periodic boundary conditions and the nutrients have Dirichlet boundary conditions, leading to a constant influx of nutrients from the boundary. The cells divide in each populated deme linearly dependent on the nutrient concentration and the current treatment state. After a defined population threshold is reached, the newly grown cells start to disperse to neighboring pixels. Under treatment the cells stop dividing. Time to progression is defined as the time point where either the colony reaches 71 mm^2 in size or the end of the simulation is reached.

Acknowledgments

The authors thank S. Aif, M. Eiche, E. Fischer, I. Schneider, and L. Strampe for valuable discussions. We are extremely grateful for the support of J. Guck and his entire division.

Funding Declaration

This work was supported by the Emmy Noether Programme of the German Research Foundation (project 455449456).

Author contributions

N.A., T.C., and J.K. conceived and designed the study. N.A. and A.P. performed experiments. T.C. performed simulations. N.A., T.C., and A.P. analyzed the data. N.A., T.C., and J.K. wrote the manuscript.

References

1. Bukowski, K., Kciuk, M. & Kontek, R. Mechanisms of multidrug resistance in cancer chemotherapy. *International journal of molecular sciences* **21,** 3233 (2020).
2. Ingham, J., Ruan, J.-L. & Coelho, M. A. Breaking barriers: we need a multidisciplinary approach to tackle cancer drug resistance. *BJC reports* **3,** 11 (2025).
3. Murray, C. J. *et al.* Global burden of bacterial antimicrobial resistance in 2019: a systematic analysis. *The lancet* **399,** 629–655 (2022).
4. Naghavi, M. *et al.* Global burden of bacterial antimicrobial resistance 1990–2021: a systematic analysis with forecasts to 2050. *The Lancet* **404,** 1199–1226 (2024).
5. Hallatschek, O. & Nelson, D. R. Life at the front of an expanding population. *Evolution* **64,** 193–206 (2010).
6. Korolev, K. S. *et al.* Selective sweeps in growing microbial colonies. *Physical biology* **9,** 026008 (2012).
7. Gralka, M. *et al.* Allele surfing promotes microbial adaptation from standing variation. *Ecology letters* **19,** 889–898 (2016).
8. Kayser, J., Schreck, C. F., Yu, Q., Gralka, M. & Hallatschek, O. Emergence of evolutionary driving forces in pattern-forming microbial populations. *Philosophical Transactions of the Royal Society B: Biological Sciences* **373,** 20170106 (2018).
9. Kayser, J., Schreck, C. F., Gralka, M., Fusco, D. & Hallatschek, O. Collective motion conceals fitness differences in crowded cellular populations. *Nature ecology & evolution* **3,** 125–134 (2019).
10. Giometto, A., Nelson, D. R. & Murray, A. W. Physical interactions reduce the power of natural selection in growing yeast colonies. *Proceedings of the National Academy of Sciences* **115,** 11448–11453 (2018).
11. Fusco, D., Gralka, M., Kayser, J., Anderson, A. & Hallatschek, O. Excess of mutational jackpot events in expanding populations revealed by spatial Luria–Delbrück experiments. *Nature communications* **7,** 12760 (2016).
12. Aif, S., Appold, N., Kampman, L., Hallatschek, O. & Kayser, J. Evolutionary rescue of resistant mutants is governed by a balance between radial expansion and selection in compact populations. *Nature communications* **13,** 7916 (2022).
13. Hallatschek, O. *et al.* Proliferating active matter. *Nature Reviews Physics* **5,** 407–419 (2023).
14. Schreck, C. F. *et al.* Impact of crowding on the diversity of expanding populations. *Proceedings of the National Academy of Sciences* **120,** e2208361120 (2023).
15. Gatenby, R. A., Brown, J. & Vincent, T. Lessons from applied ecology: cancer control using an evolutionary double bind. *Cancer research* **69,** 7499–7502 (2009).
16. Gatenby, R. A. & Brown, J. S. Integrating evolutionary dynamics into cancer therapy. *Nature reviews Clinical oncology* **17,** 675–686 (2020).
17. Enriquez-Navas, P. M. *et al.* Exploiting evolutionary principles to prolong tumor control in preclinical models of breast cancer. *Science translational medicine* **8,** 327ra24–327ra24 (2016).
18. Zhang, J., Cunningham, J. J., Brown, J. S. & Gatenby, R. A. Integrating evolutionary dynamics into treatment of metastatic castrate-resistant prostate cancer. *Nature communications* **8,** 1816 (2017).
19. Kim, E., Brown, J. S., Eroglu, Z. & Anderson, A. R. Adaptive therapy for metastatic melanoma: predictions from patient calibrated mathematical models. *Cancers* **13,** 823 (2021).
20. Hockings, H. *et al.* Adaptive therapy achieves long-term control of chemotherapy resistance in high grade ovarian cancer. *bioRxiv* (2023).
21. Brady-Nicholls, R. & Enderling, H. Range-bounded adaptive therapy in metastatic prostate cancer. *Cancers* **14,** 5319 (2022).

22. Bacevic, K. *et al.* Spatial competition constrains resistance to targeted cancer therapy. *Nature communications* **8,** 1995 (2017).

23. Noble, R. *et al.* Spatial structure governs the mode of tumour evolution. *Nature ecology & evolution* **6,** 207–217 (2022).

24. Strobl, M. A. *et al.* Spatial structure impacts adaptive therapy by shaping intra-tumoral competition. *Communications medicine* **2,** 46 (2022).

25. Gallaher, J. A., Enriquez-Navas, P. M., Luddy, K. A., Gatenby, R. A. & Anderson, A. R. Spatial heterogeneity and evolutionary dynamics modulate time to recurrence in continuous and adaptive cancer therapies. *Cancer research* **78,** 2127–2139 (2018).

26. Gallaher, J. *et al.* Intermetastatic and intrametastatic heterogeneity shapes adaptive therapy cycling dynamics. *Cancer Research* **83,** 2775–2789 (2023).

27. Maltas, J. *et al.* Drug dependence in cancer is exploitable by optimally constructed treatment holidays. *Nature ecology & evolution* **8,** 147–162 (2024).

28. Lewinsohn, M. A., Bedford, T., Müller, N. F. & Feder, A. F. State-dependent evolutionary models reveal modes of solid tumour growth. *Nature Ecology & Evolution* **7,** 581–596 (2023).

29. Algazi, A. P. *et al.* Continuous versus intermittent BRAF and MEK inhibition in patients with BRAF-mutated melanoma: a randomized phase 2 trial. *Nature medicine* **26,** 1564–1568 (2020).

30. Berg, S. *et al.* Ilastik: interactive machine learning for (bio) image analysis. *Nature methods* **16,** 1226–1232 (2019).